

## Application of synchrotron X-ray imaging to phase objects in orthopedics

K. Mori,<sup>a,b\*</sup> N. Sekine,<sup>a</sup> H. Sato,<sup>a</sup> D. Shimao,<sup>b</sup>  
H. Shiwaku,<sup>c</sup> K. Hyodo,<sup>d</sup> H. Sugiyama,<sup>d,e</sup> M. Ando,<sup>d,e</sup>  
K. Ohashi,<sup>f</sup> M. Koyama<sup>f</sup> and Y. Nakajima<sup>f</sup>

<sup>a</sup>Department of Radiological Sciences, Ibaraki Prefectural University of Health Sciences, Ami 4669-2, Inashiki, Ibaraki 300-0394, Japan, <sup>b</sup>Graduate School of Health Sciences, Ibaraki Prefectural University of Health Sciences, Ami 4669-2, Inashiki, Ibaraki 300-0394, Japan, <sup>c</sup>Synchrotron Radiation Research Center, Kansai Research Establishment, JAERI, Kouto 1-1-1, Sayo, Hyogo 679-5198, Japan, <sup>d</sup>Photon Factory, Institute of Material Structure Sciences, High Energy Accelerator Research Organization, Oho 1-1, Tsukuba, Ibaraki 305-0801, Japan, <sup>e</sup>Department of Photon Science, School of Advanced Studies, Graduate University for Advanced Studies, Shonan International Village, Hayama, Miura, Kanagawa 240-0193, Japan, and <sup>f</sup>Department of Radiology, St Marianna University School of Medicine, Miyamae 2-16-1, Kawasaki, Kanagawa 216-8511, Japan. E-mail: mori@ipu.ac.jp

Novel imaging of the fine structures of the ribs of a pig and a specimen of human osteosarcoma utilizing the spatial coherence of X-rays was successfully performed with an incident X-ray energy of 30 keV at SPring-8, Japan. The image contrast appearing at the periphery of trabecular bone, small calcifications and small fractures is caused by the phase shift of the X-rays at the boundary of these objects that have different X-ray refractive indices. The image is recorded on mammography film without an intensifying screen. Comparison of the image contrast using different sample-to-film distances,  $Z$ , such as  $Z = 5$  m and  $Z \simeq 0$  m, showed that the former images were always more informative, *i.e.* better in resolution and/or image contrast when imaging trabecular bone, bone marrow and small fractures in compact bone, and for imaging cartilage. Radiography using synchrotron X-rays for phase objects should be a powerful tool for diagnosis in orthopedics, especially for bone disease.

**Keywords:** bone imaging; small fractures; phase objects; coherence; X-ray refraction contrast.

### 1. Introduction

Since the discovery of X-rays in 1895 up until recently, all practical methods of radiography for human imaging have been based on X-ray absorption contrast (Röntgen, 1896; Clark, 1986). The image contrast of this method can be explained by alteration of the amplitude of the X-ray wave when an object is placed before it. Recently, novel imaging methods have been developed with synchrotron X-ray sources and microfoc tubes that provide highly coherent X-rays at the observation point (Snigerev *et al.*, 1995; Cloetens *et al.*, 1995; Wilkins *et al.*, 1996; Spanne *et al.*, 1999). The image contrast of this method can be explained by the shift of the phase of the X-ray wave when different objects are placed before it, *i.e.* the incident X-ray refraction at the boundary of objects or X-ray diffraction at a fine fissure such as a small fracture within phase objects that have different X-ray refractive indices. The image of the object as recorded on an X-ray film is enhanced by white–black fringe

contrast (Somenkov *et al.*, 1991; Baruchel, 1996). This image enhancement allows good visibility of the boundary between low-density materials or of line-shaped structures. A synchrotron source is suitable for practical radiography of phase objects because it produces a high degree of spatial coherence of incident X-rays with high intensity. Sufficient size of exposure field for human imaging is obtained by X-ray diffraction techniques with asymmetric-cut silicon crystals. Radiography of phase-objects in orthopedics using monochromatic synchrotron X-rays has been developed by Mori *et al.* (1999).

In the following, an experimental procedure for imaging fine structures of bone using synchrotron X-rays is described. A brief discussion will be given on the difference of the image quality using different sample-to-film distances for bone specimens with bone disease or degeneration such as small fractures in the compact bone and cartilage, calcification, and fine structure of human osteosarcoma.

### 2. Experimental procedure

Simplified imaging processes of radiography for a phase object are described in Figs. 1(a) and 1(b). As shown in Fig. 1(a), the incident X-ray is refracted at the boundary of the objects that have different refractive indices for X-rays. The refracted X-ray appears on the film in the neighbourhood of the position of the undeviated ray. The image contrast is strongly dependent on the sample-to-film distance,  $Z$ . The refracted X-ray is displaced away from the undeviated ray with increasing  $Z$ . Regions of lower X-ray dose appear as bright areas and those of higher X-ray dose as dark areas resulting in white–black fringe contrast on the film. The image contrast using highly coherent X-rays increases for suitable  $Z$  values. For example, the image contrast at  $Z = 0$  is purely absorptive, so the contrast is lower than that for larger  $Z$  because the bright and dark areas are undeviated on the film. This imaging model is suitable for explaining the image contrast at the edge of trabecular bone or small calcifications acting as phase objects.

In the case of a small fracture, the shape of the section is considered as a concavity with aperture size  $A$  and depth  $L$  whose inside is filled with blood or lymph as shown in Fig. 1(b). From the point of view of the phase shift ( $\varphi$ ) of the X-ray, the concavity can be divided into two parts: the upper one is a single-slit shape with aperture size  $A$  and width  $L$  with the phase shift between the X-rays at the slit blades and the slit opening; the lower one is a rectangle without the phase shift between the X-rays (Mori, Sekine *et al.*, 2000). The image contrast of a small fracture as a phase object can be explained by X-ray diffraction at a semitransparent single slit as shown in Fig. 1(b). The resulting phase shift between the slit blades and slit opening is expressed as

$$\varphi = 2\pi(\Delta n)L/\lambda, \quad (1)$$

where  $\Delta n = n_2 - n_1$  is the difference in the X-ray refractive indices between  $n_2$  for the slit blades and  $n_1$  for the slit opening,  $L$  is the width of the blades corresponding to the depth of the fissure, and  $\lambda$  is the wavelength of the X-rays. It is known that the refractive index of the medium  $n = 1 - \delta$ , where  $\delta$  is the unit decrement of the refractive index that is proportional to the medium density  $\rho$ , as follows (Ingal *et al.*, 1998),

$$\delta \simeq 1.35 \times 10^{-7} \rho \lambda^2, \quad (2)$$

where  $\rho$  is expressed in  $\text{kg m}^{-3}$  and  $\lambda$  in nm. In the case of small fractures in compact bone at  $\lambda = 0.041$  nm ( $E = 30$  keV), calculated values of  $\delta$  for compact bone and blood (lymph) are about  $4.36 \times 10^{-7}$  and  $2.41 \times 10^{-7}$ , respectively, where the densities of compact

bone and blood (lymph) are taken as 1920 and 1060, respectively. If we assume that  $L \simeq 100 \mu\text{m}$ , the aperture size  $A$  is from  $20 \mu\text{m}$  to  $30 \mu\text{m}$  and  $Z = 5 \text{ m}$ , the calculated phase shift  $\varphi$  is about  $-\pi$ , from which the main image contrast of the fracture by the calculation based on Fresnel diffraction of X-rays would be white–black–white on the film.

The degree of X-ray coherence is defined by the spatial coherence length,  $d$ , as defined in the following way,

$$d = \lambda l / \sigma, \quad (3)$$

where  $\lambda$  is the wavelength of the X-rays,  $l$  is the source-to-observation distance and  $\sigma$  is the source size. The longer  $l$  and the smaller  $\sigma$  are, the better the conditions for generating higher coherence of the

incident X-ray beam. This means better image contrast of phase objects.

The radiography uses the synchrotron X-rays produced by BL20B2 of SPring-8, that operates with an acceleration energy of 8 GeV and an initial recorded current of 100 mA. The experimental apparatus for the radiography is shown schematically in Fig. 2. The images were recorded on mammography film (Kodak Min-R 2000) without an intensifying screen. The samples were a specimen of osteosarcoma, developed on the distal end of a human femur with a slice thickness of 5 mm, and raw ribs of a LWD-pig, Landrace-Yorkshire-Duroc (Large White), whose sizes were 10–15 mm in diameter and about 200 mm in length (Mori *et al.*, 2001). These dimensions are about the same as those of human ribs or fingers. About one day before the radiography was carried out, the middle of the sample surface was hit with a plastic hammer and/or the distal end of the sample (cartilage) was strongly bent to form small fractures. The samples were located about 200 m from the source. The size of the exposure field was 45 mm horizontally and 25 mm vertically. The maximum field length in the horizontal direction was 150 mm in the present design. Incident X-rays of energy 30 keV were used since this value is the same as the effective energy used in clinical radiography for the hand or finger-sized bones.

### 3. Results and discussion

Typical values of  $Z$  for seeing a clear fracture line, bone trabecular and calcification as found from the experiment were from 0.5 m to over 7 m with an incident X-ray energy of 30 keV (Mori, Shikano & Shiwaku, 2000). X-ray images at the middle of the rib recorded using synchrotron X-rays at  $Z \simeq 5 \text{ m}$  and  $Z \simeq 0 \text{ m}$  are shown in Figs. 3(a)–(c) and Fig. 3(d), respectively. X-ray images of the distal end of the rib recorded using synchrotron X-rays at  $Z \simeq 5 \text{ m}$  and  $Z \simeq 0 \text{ m}$  are shown in Figs. 4(a) and 4(b), respectively. X-ray images of the distal end of another rib sample recorded using synchrotron X-rays at  $Z \simeq 5 \text{ m}$  and  $Z \simeq 0 \text{ m}$  are shown in Figs. 5(a) and 5(b), respectively. X-ray images of the specimen of human osteosarcoma recorded using synchrotron X-rays at  $Z \simeq 5 \text{ m}$  and  $Z \simeq 0 \text{ m}$  are shown in Figs. 6(a) and 6(b), respectively. The exposure time ranged from 500 mA s to 1000 mA s for figure parts (a) and (b), respectively.

Figs. 3(a)–(c) and 3(d) reveal some characteristics of the X-ray images of phase objects such as the periphery of trabecular bone and small fractures in compact bone. In the refraction-contrast image at

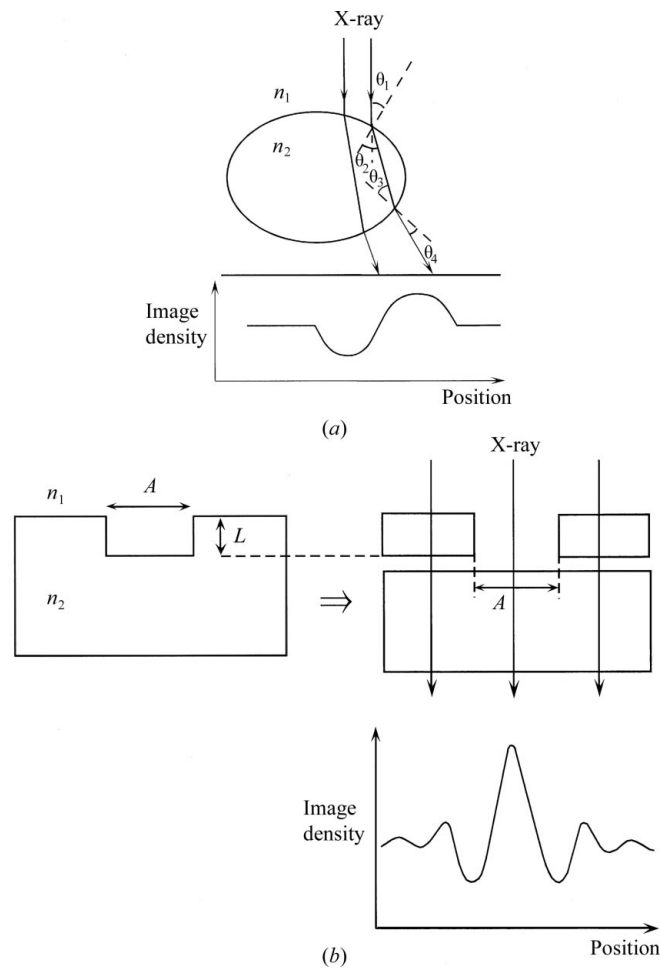


**Figure 1**  
(a) Imaging process of the radiography for trabecular bone. The incident X-ray is refracted at the boundary of the objects that have different refractive indices for X-rays according to Snell's law. When the refractive index of X-rays for bone marrow,  $n_1$ , is greater than that for compact or trabecular bone,  $n_2$ , there follow relationships between angles of incidence and refraction:  $\theta_1 < \theta_2$  and  $\theta_3 > \theta_4$ . The broken lines are the normal to the sample surface. Typical intensity distribution on the film is also shown in the figure; higher image intensity corresponds to a darker area on the film. (b) Imaging process of radiography for a small fracture. The phase shift of the X-rays arises at the region within depth  $L$  from the surface. X-rays penetrating the semitransparent single slit interfere and cause the interference fringe on the film. Typical intensity distribution on the film is shown in the figure. The intensity distribution was well explained by Fresnel diffraction of X-rays. The definition of the image densities was the same as for (a).

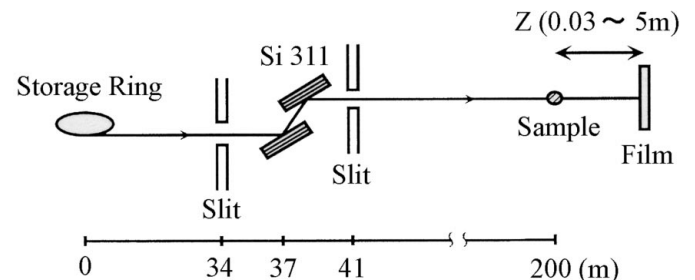


**Figure 2**  
Experimental apparatus (schematic) of the radiography at BL20B2 of SPring-8. The Si 311 double-crystal monochromator in (+, -) arrangement was located about 37 m from the source. The source size at the bending magnet was  $290 \mu\text{m}$  in the horizontal and  $44 \mu\text{m}$  in the vertical direction. These values are the sum of  $1\sigma$  of each side of the intensity distribution that is defined in a Gaussian curve (Soutome *et al.*, 1999; Tanaka *et al.*, 2000). Using expression (3), the calculated coherence length of the incident X-ray beams is  $29 \mu\text{m}$  horizontally and  $187 \mu\text{m}$  vertically at 30 keV. Here,  $l = 200 \text{ m}$  is used for the observation distance. The image contrast is strongly dependent on the sample-to-film distance,  $Z$ .

$Z \simeq 5$  m, white–black contrast can be seen at the periphery of the trabecular bone as shown in Fig. 3(b). This was not observable in the absorption-contrast image recorded using synchrotron X-rays at  $Z \simeq 0$ . The white–black contrast allows for easier determination of the configuration of the trabecular bone in the refraction-contrast image compared with the absorption-contrast image recorded using synchrotron X-rays. That the black line appears at the outermost limit of the trabecular bone is an indication that the refractive index of the trabecular bone is smaller than that of the surrounding bone marrow for 30 keV X-rays. This can also be understood from the fact that the density of trabecular bone is higher than that of the bone marrow. The image recorded using synchrotron X-rays at  $Z \simeq 5$  m is superior

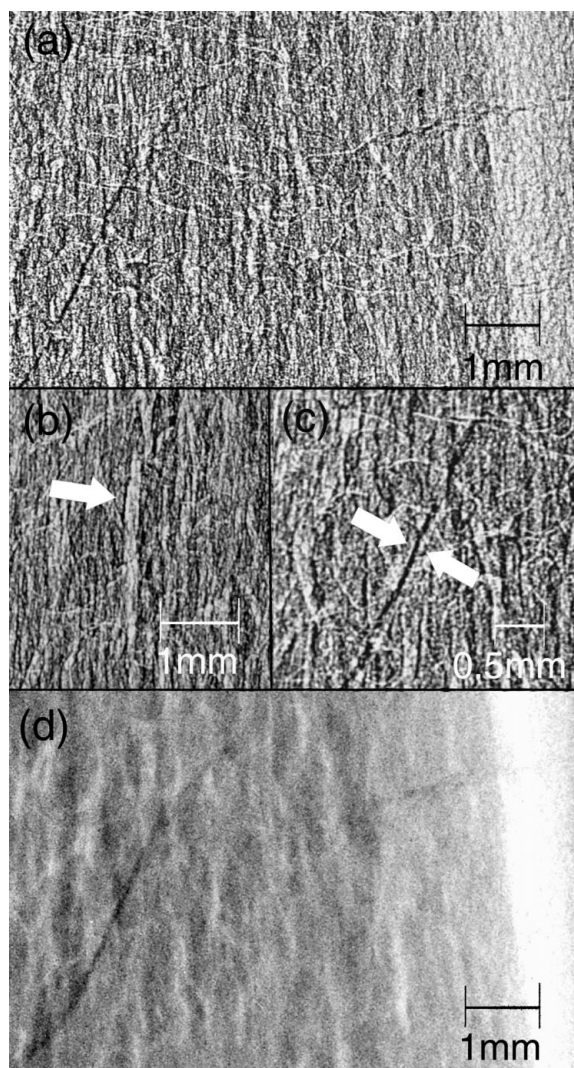


**Figure 3**

X-ray images at the middle of the rib recorded using synchrotron X-rays. (a), (b) and (c). Images recorded using synchrotron X-rays at  $Z \simeq 5$  m. The refraction-contrast image of the trabecular bone with white–black contrast ( $\rightarrow$ ) on the film is shown in (b), the image of a small fracture with white–black–white contrast ( $\rightarrow$ ) on the film is shown in (c) (Mori, Shikano, Sato *et al.*, 2000). (d) X-ray absorption-contrast image recorded using synchrotron radiation at  $Z \simeq 0$  m. The rib sample without surrounding soft tissue packed in a transparent plastic bag was used for imaging. The sample has a small fracture in the middle. The fractures running horizontally and transversely are clearly seen in (a), and less so in (d). The trabecular bone, important in the diagnosis of bone diseases, was also clearly observed in (a).

to the absorption-contrast image recorded using synchrotron X-rays at  $Z \simeq 0$  m for the purposes of delineating the minute changes in the trabecular bone.

In terms of delineating small fractures, the white–black–white contrast ( $\rightarrow$ ) appears along the fissure in the image recorded at  $Z \simeq 5$  m as shown in Fig. 3(c). This contrast makes the image of the fracture line clearer compared with that in the absorption-contrast image recorded at  $Z \simeq 0$  m. By using a magnifier with a scale, the width of the fissure on the bone surface is found to be about 30  $\mu$ m. This result is in good agreement with the calculated values giving white–black–white contrast on the film. Thus, it is conceivable that the image recorded using synchrotron X-rays at  $Z \simeq 5$  m is superior to the absorption-contrast image recorded using synchrotron X-rays at  $Z \simeq 0$  m in the precise delineation of small fractures. The delineation of such features in phase-object imaging is particularly useful for capturing small fractures in the bone periphery, in areas that are targets for tangential projection of synchrotron X-rays.

Figs. 4(a) and 4(b) shed light on the characteristics of the X-ray image of a phase object such as a fracture generated in the distal end of the cartilage of a rib. In Fig. 4(a) the fracture line can be observed in the centre of the image ( $\rightarrow$ ). As shown in Fig. 4(b), diagnosis of a cartilage fracture would be difficult using the absorption-contrast image recorded using synchrotron X-rays at  $Z \simeq 0$  m.

The X-ray image has generated line images at the borders between air and soft tissue, and between soft tissue and cartilage. These lines allow for sharper delineation of tissue configuration in the refraction-contrast image compared with the absorption-contrast image. Unlike the white–black contrast seen in Fig. 3(a), most of the prominent features are single white lines. These lines are probably attributable to the surface of the sample specimen having a lower degree of uniformity of the borders between air and soft tissue, and between soft tissue and cartilage, compared with the border between trabe-

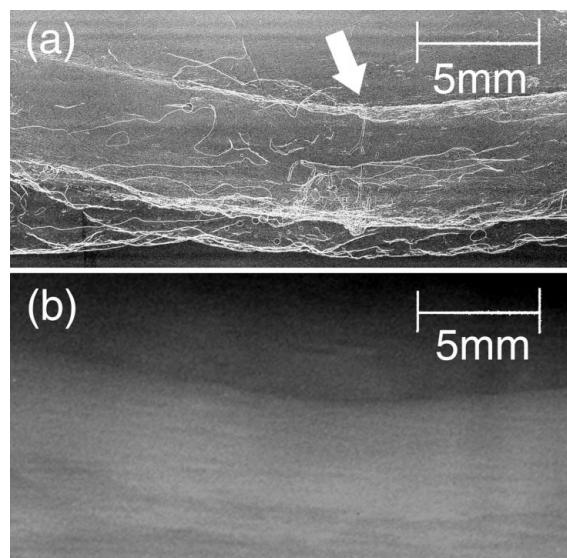


**Figure 4**

X-ray images of the distal end of the rib recorded using synchrotron X-rays. (a) X-ray image recorded using synchrotron X-rays at  $Z \simeq 5$  m. (b) Absorption-contrast image recorded using synchrotron X-rays at  $Z \simeq 0$  m. The cartilage sample with surrounding soft tissue packed in a transparent plastic bag was used for imaging. The sample has a small fracture in the middle. The fractures running vertically are clearly seen in (a), and much less so in (b). The white curves overlapping the cartilage image as shown in (a) were caused by the soft tissue lump on the sample surface.

cular bone and bone marrow. That is, it is likely that the broad tissue borders viewed from the source generating X-ray refractions resulted in a wide area reached by refracted X-rays on the film, which prevented the appearance of a distinct black line on the film. Even in these kinds of cases, the image recorded using synchrotron X-rays at  $Z \approx 5$  m is extremely sharp compared with the absorption-contrast image recorded using synchrotron X-rays at  $Z \approx 0$  m.

The rib sample used in Fig. 5 was larger compared with the specimen used in Fig. 4. The image resolution of the borders between air and soft tissue and between soft tissue and cartilage, in Figs. 5(a) and 5(b), was similar to that of Fig. 4. Calcification was observed in the central portion of the cartilage in this specimen. The image showed age-induced changes of cartilage into hard bone. The refraction-contrast image recorded using synchrotron X-rays at  $Z \approx 5$  m gives a high definition picture of the microstructure of the calcified region. The absorption-contrast image recorded using synchrotron X-rays at  $Z \approx 0$  m was unable to delineate the microstructure of this region. During the healing process of bone fractures or bone defects, a proliferation of bone-forming cells occurs around

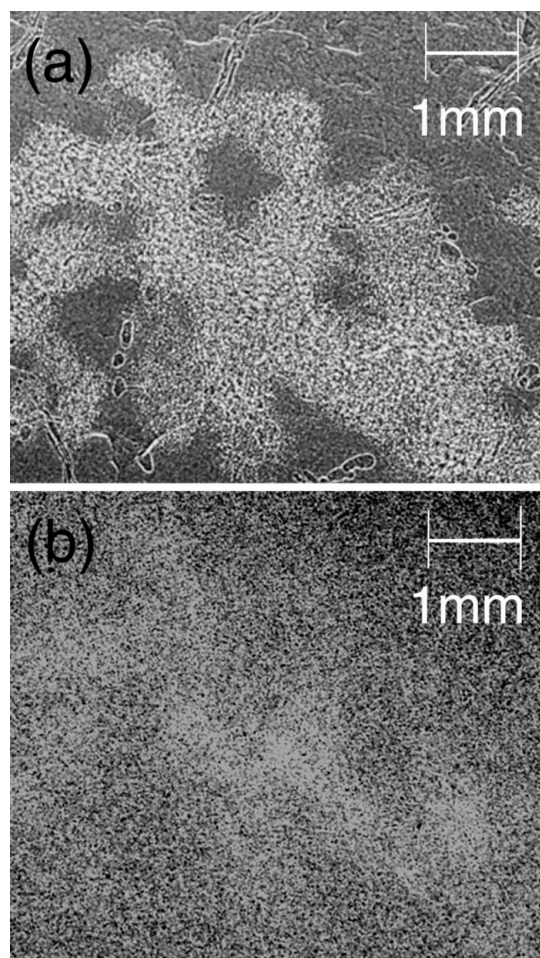


**Figure 5**  
X-ray images of the distal end of the rib recorded using synchrotron X-rays. (a) X-ray image recorded using synchrotron X-rays at  $Z \approx 5$  m. (b) Absorption-contrast image recorded using synchrotron X-rays at  $Z \approx 0$  m. The cartilage sample with surrounding soft tissue packed in a transparent plastic bag was used for imaging. Observation of a section of the cartilage; calcification was observed in the central portion of the specimen. This is clearly observed in (a), and less so in (b).

the site, and then these cells differentiate into osteoblasts and chondrocytes to develop into tissue consisting of fibrous bone and cartilage. In X-ray photographs, these newly formed tissues are represented as callus images. Refraction-contrast imaging should allow for more sensitive delineation of the process of callus formation compared with absorption-contrast imaging. Such images should aid in more accurate delineation and diagnosis of the state of healing of bone diseases as well as of changes over time of metabolic bone diseases.

Figs. 6(a) and 6(b) are images taken of a specimen of osteosarcoma. The configuration of trabecular bone and the distribution of bone marrow are more minutely delineated in the refraction-contrast image compared with the absorption-contrast image. There is more minute delineation of the manner in which the osteosarcoma has destroyed the trabecular bone and has infiltrated into the medullary cavity, *i.e.* of the distribution of the sarcoma. Use of refraction-contrast imaging should also allow for more accurate delineation of the distribution of malignant neoplasms compared with the conventional method.

As outlined above, X-ray images recorded with synchrotron X-rays at 30 keV of porcine ribs (compact bone and cartilage) and of a human osteosarcoma specimen demonstrated a superior degree of image delineation (contrast and spatial resolution) of trabecular

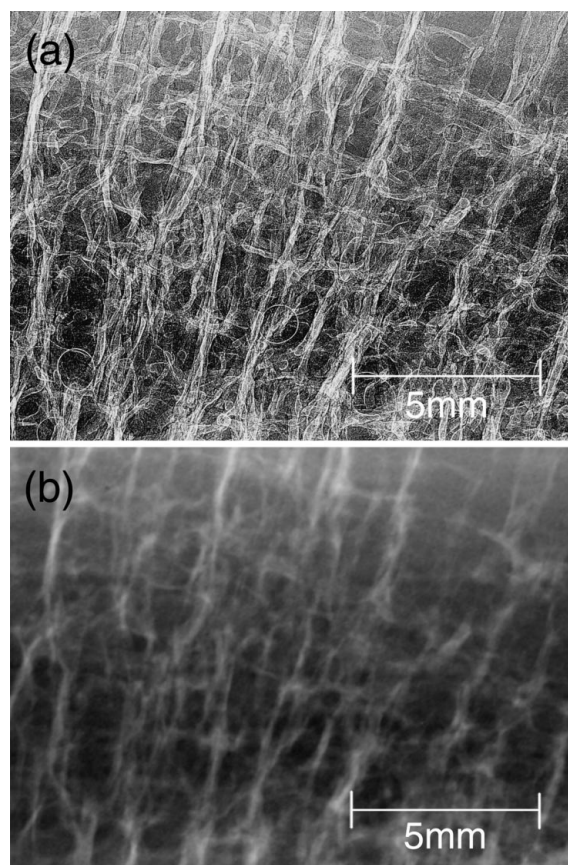


**Figure 6**  
X-ray images of a specimen of human osteosarcoma recorded using synchrotron X-rays. (a) X-ray image recorded using synchrotron X-rays at  $Z \approx 5$  m. (b) Absorption-contrast image recorded using synchrotron X-rays at  $Z \approx 0$  m. The specimen of human osteosarcoma whose thickness was 5 mm was packed into an acrylic box with formalin.

bone, small fractures, bone-marrow tissue and cartilage compared with the absorption-contrast image recorded with synchrotron X-rays.

In terms of the radiographic geometry, the factor characterizing the new method compared with the conventional method is that there is a larger distance between the sample and the imaging device. As the synchrotron X-ray beams have good parallelism (low divergence), there is virtually no enlargement of the image, relative to the sample, in this geometry. The ability to obtain images that are equal to the actual size of the object has significance in terms of diagnostic imaging, as it is possible to ascertain from the image any changes in size or distance. In addition, improvement of image contrast due to the air gap can be expected even without the use of anti-scatter grids. If it is possible to perform radiographic imaging without the use of these grids, it should then become feasible to reduce the necessary radiation (dose) to a fraction of that required in the conventional method. The degree of reduction in exposure is likely to be larger for thick objects, where high-energy X-rays are used. In future, as the spatial resolution is improved by such electronic imaging devices as imaging plates, flat-panel detectors and X-ray CCD cameras, it should become possible to use the synchrotron X-ray imaging for phase objects to obtain human images of high diagnostic value in the radiographic assessment of bone and soft-tissue diseases.

This work has been carried out according to the SPring-8 proposal No. 2001A0468-NL-np and with financial support provided from a Grant-in-Aid for Scientific Research (C).

## References

- Baruchel, J. (1996). *X-ray and Neutron Dynamical Diffraction Theory and Application*, edited by A. Authier, pp. 207–209. New York: Plenum.
- Clark, K. C. (1986). *Positioning in Radiography*, edited by R. A. Swallow, p. 326. Oxford: Butterworth Heinemann.
- Cloetens, P., Barrett, R., Baruchel, J., Guigay, J.-P. & Schlenker, M. (1995). *J. Phys. D*, **29**, 133–146.
- Ingal, V. N., Beliaevskaya, E. A., Brianskaya, A. P. & Merkurieva, R. D. (1998). *Phys. Med. Biol.* **43**, 2555–2567.
- Mori, K., Hyodo, K., Shikano, N. & Ando, M. (1999). *Jpn. J. Appl. Phys.* **38**, L1339–L1341.
- Mori, K., Sato, H., Sekine, N., Shikano, N., Shiwaku, H., Ohashi, K., Koyama, M. & Nakajima, Y. (2001). *SPring-8 User Experiment Report 2001A*. Vol. 5. SPring-8, Hyogo, Japan.
- Mori, K., Sekine, N., Sato, M., Sato, H., Shikano, N., Igarashi, T., Hyodo, K. & Ando, M. (2000). *Acta Sci. VPI*, **5**, 47–52.
- Mori, K., Shikano, N., Sato, M., Sato, H., Sekine, N., Shiwaku, H., Hyodo, K., Sugiyama, H., Ando, M. & Uyama, C. (2000). *Med. Imag. Tech.* **18**, 441–442.
- Mori, K., Shikano, N. & Shiwaku, H. (2000). *SPring-8 User Experiment Report 1999B*, Vol. 4, p. 110. SPring-8, Hyogo, Japan.
- Röntgen, W. C. (1896). *Nature (London)*, **53**, 274–277.
- Snigirev, A., Snigireva, I., Kohn, V., Kuznetsov, S. & Schelokov, I. (1995). *Rev. Sci. Instrum.* **66**, 5486–5492.
- Somenkov, V. A., Tklich, A. K. & Shil'shtein, S. Sh. (1991). *Sov. Phys. Tech. Phys.* **36**, 1309–1311.
- Soutome, K., Tanaka, H., Takano, M., Kumagai, K., Ohkuma, H. & Kumagai, N. (1999). *SPring-8 Annual Report*, pp. 136–138. SPring-8, Hyogo, Japan.
- Spanne, P., Raven, C., Snigireva, I. & Snigirev, A. (1999). *Phys. Med. Biol.* **44**, 741–749.
- Tanaka, H., Kumagai, K., Masaki, M., Ohkuma, H., Soutome, K., Takao, M. & SPring8/JASRI (2000). *Proceedings of the 7th European Particle Accelerator Conference*, Vienna, Austria, pp. 1575–1577.
- Wilkins, S. W., Gureyev, T. E., Gao, D., Pogany, A. & Stevenson, A. W. (1996). *Nature (London)*, **384**, 335–338.